Orientational Proliferation and Successive Twinning from Thermoreversible Hexagonal−Body-Centered Cubic Transitions

Hee Hyun Lee,† Woon-Yong Jeong, and Jin Kon Kim*

Department of Chemical Engineering and Polymer Research Institute, Electronic and Computer Engineering Divisions, Pohang University of Science and Technology, Kyungbuk 790-784, Korea

Kyo Jin Ihn

Department of Chemical Engineering, Kangwon National University, Chunchon 200-701, Korea

Julia A. Kornfield and Zhen-Gang Wang

Department of Chemical Engineering, California Institute of Technology, Pasadena, California 91125

Shuyan Qi

Department of Chemical Engineering, University of California, Berkeley, California 94710

Received May 31, 2001; Revised Manuscript Received September 7, 2001

ABSTRACT: The deterministic proliferation of the orientation of hexagonally packed cylinders (HEX) from the twinned body-centered cubic (BCC) phase is investigated by synchrotron small-angle X-ray scattering (SAXS) and rheo-optical methods for di- and triblock copolymers of styrene and isoprene (SI and SIS). Repeated heating and cooling cycles starting from an initially aligned HEX produce a proliferation of cylinder orientations from successively twinned BCC states. The evolution of the orientation distribution of HEX cylinders produces a decrease in the birefringence and increase in the modulus with each successive generation. The cylinder axes of the degenerate HEX states coincide with the ⟨111⟩ directions of the twinned BCC due to the epitaxial growth of cylinders from the twinned BCC. The distribution of the cylinder axes of the degenerate HEX states among the ⟨111⟩ directions of the twinned BCC is found to be affected by memory of the prior HEX state, which decays with annealing time in the BCC state.

1. Introduction

Controlling nanostructure in materials has attracted intense interest because of its relevance to technologies ranging from biomedicine to photonics. Macroscopic alignment of self-assembled nanostructures in soft materials can be induced by applied fields, especially flow. Here we demonstrate that an initially flow-induced orientation can provide a platform for generating distinct orientation distributions by thermal treatments that take the material back and forth across an order−order transition. The orientation distributions accessed in this way cannot be generated directly by any other methods.

Specifically, we show that, starting from a single orientation of the hexagonal cylinder (HEX) phase of an AB or ABA block copolymer, repeated heating and cooling cycles across the transition boundary between the HEX and the body-centered-cubic (BCC) sphere phases lead to continued proliferation of the HEX orientation and successive twinning of the BCC structure. To our knowledge, the phenomenon we report is the first example of deterministic proliferation of orientation of an ordered structure in either soft-condensed materials or crystalline solids. This phenomenon requires a special crystallographic relationship between two ordered phases connected by an order−order transition. The two ordered phases must each produce, in a deterministic manner, more than one orientation from a single orientation upon the transition from one to the other, and these multiple orientations must not form a closed set through repeated heating/cooling cycles across the transition boundary. Nondeterministic proliferation occurs when one of the order−order transitions produces a continuous distribution of orientations, for example, the lamellae (LAM) to HEX transition in block copolymers: a single orientation of LAM produces HEX orientations that are completely random in the azimuth angle about the LAM normal. A lack of proliferation occurs when the orientations probed by the order−order transition form a closed set; for example the transition between the cubic and tetragonal phases in crystalline solids involves three orientations of the tetragonal phase, all of which map back onto the single orientation of the original cubic phase, so repeated heating/cooling across the transition does not lead to any new orientations.

The crystallographic relation between two ordered phases of block copolymers connected by an order−order transition is known as epitaxy.[1−4] In the case of the HEX → BCC transition, epitaxy dictates that one of the ⟨111⟩ directions of the BCC phase coincides with that of the cylinder axis of the original HEX, while the other three

* To whom correspondence should be addressed: e-mail jkkim@postech.ac.kr.

† Present address: Advanced Materials Research Institute, LG Chemical Ltd., Research Park, 104-1, Yuseong Science Town, Taejon, South Korea, 305-380.

10.1021/ma010951c CCC: $22.00
Published on Web 01/03/2002

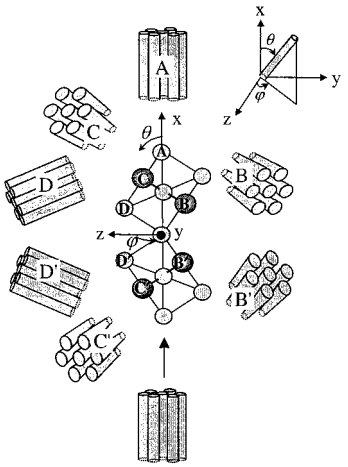

Figure 1. Schematic of the transition: HEX-0 → twinned BCC-I → HEX-I.

⟨111⟩ directions form the skeletons of a tetrahedron with the first, with their azimuth orientation conforming to the hexagonal symmetry of the cylinders. Furthermore, it was both predicted theoretically[5] and demonstrated experimentally[6,7] that the transition from HEX to BCC should yield two BCC structures connected by twinning as opposed to a single BCC. Upon the reverse transition, each of the ⟨111⟩ directions of the BCC can become the cylinder axis in the HEX phase. Since there are four equivalent ⟨111⟩ directions in each of the BCC twins, with one of the four (along the initial cylinder orientation) shared by both, seven distinct HEX orientations are to be expected after one HEX → twinned BCC → HEX cycle (Figure 1). However, the anticipated multiplicity of the HEX orientations during the BCC to HEX transition was not reported in earlier studies by Koppi et al.[1] for a poly(ethylene-*alt*-propylene)-*block*-poly(ethylethylene) (PEP−PEE) diblock copolymer or by Kimishima et al.[8] for a polystyrene-*block*-polyisoprene (SI) diblock copolymer.

In this paper, we provide clear small-angle X-ray scattering (SAXS) evidence showing the generation of seven cylinder directions upon cooling the twinned BCC phase back into HEX. We further demonstrate that repeated heating and cooling cycles lead to continued proliferation of HEX orientations and successive twinning as a result of the multiplicity of HEX orientations produced during each HEX → twinned BCC → HEX cycle. This continued proliferation requires that each cooling cycle produces *new* cylinder orientations not already present in the previous generation. If the HEX to BCC transition yielded only one BCC structure, then only the first reverse transition would give new cylinder orientations; repeated heating/cooling would not yield any new cylinder orientations since the four directions form a closed set. Therefore, the fact that the HEX produces a twinned BCC is essential for the subsequent proliferation of cylinder directions and successive twinning of the BCC during repeated heating/cooling cycles. Since the epitaxial relation between the HEX and the gyroid phases is similar to that between HEX and BCC, we anticipate a similar phenomenon in the HEX ↔ gyroid transition.

Our study shows that there is a strong memory of the HEX orientation from one generation to the next, which decays with annealing time in the BCC phase. This memory effect may explain the apparent discrepancy between the present findings and those of the previous studies.[1,8]

Table 1. Molecular Characteristics and T_{OOT} of Samples Used in This Study

sample code	total MW,[a] g/mol	PS,[b] wt %	M_w/M_n[c]	T_{OOT} (°C)
Vector 4111	143 000	18.3	1.11	185 ± 1
SI-C1	67 200	18.5	1.02	182 ± 1

[a] By LALLS (low-angle laser light scattering). [b] By ^{1}H NMR. [c] By GPC calibrated with PS standard.

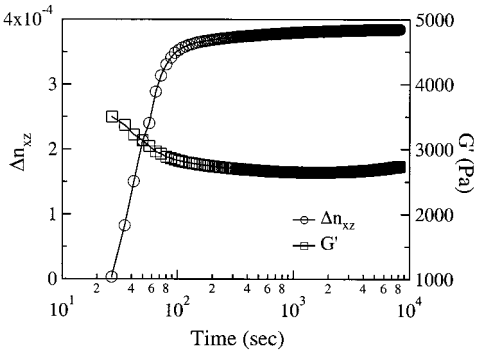

Figure 2. Change of the birefringence and storage modulus with time during LAOS with $\omega = 1$ rad/s and $\gamma_0 = 100\%$.

2. Experimental Section

Materials. We use a commercial-grade SIS triblock copolymer, Vector 4111 (Dexco Polymers Co.), whose phase behavior has been studied previously.[4] An SI diblock copolymer, SI-C1, was synthesized by anionic polymerization in cyclohexane (Aldrich Chemical Co.) with s-BuLi as an initiator at 40 °C under purified argon.[9] The diblock is matched to almost half of the triblock, and the two have nearly the same T_{OOT} for the HEX−BCC transition (Table 1). We employed both SIS triblock and SI diblock copolymers in order to compare with previous studies of diblocks of PEP−PEE[1] and SI.[8] We found that the qualitative features of orientation proliferation are similar in the diblock and triblock systems; we primarily show results for the SIS triblock copolymer in this paper.

The samples for rheology, birefringence, and SAXS experiments were prepared by solvent casting from toluene (10 wt %) in the presence of an antioxidant (Irganox 1010, Ciba-Geigy Group), followed by annealing at 130 °C for 48 h in a vacuum oven. Although toluene is a slightly better solvent for PS than for PI, the HEX ordered structure after annealing shows no evidence of a solvent effect. This sample is referred to as an as-cast sample. Well-aligned HEX cylinders were obtained from the as-cast sample by imposing a large-amplitude oscillatory shear (LAOS) with $\omega = 1$ rad/s and 100% strain amplitude at 170 °C, a temperature between the T_g of the styrene-rich domains and the T_{OOT} of the HEX−BCC transition. The LAOS was done with 50 mm diameter parallel plates in a Rheometrics RDS-II with nitrogen purge for 2.5 h until the birefringence and storage modulus, G', reached steady-state values (Figure 2). The sample was rapidly cooled (reaching ambient temperature in less than 1 min) immediately after LAOS to quench the well-aligned state.

Synchrotron Small-Angle X-ray Scattering. The SAXS measurements with synchrotron radiation were conducted at the 3C2 and 4C1 beam lines at the Pohang Light Source (PLS), Korea.[10] The wavelength of the primary beam (0.1598 nm, photon energy of 7.76 keV) was selected by use of a monochromator consisting of two Si(111) single crystals, and then was focused on a CCD detector plane by a bent cylindrical mirror. The rectangular bars are cut from each quenched specimen at a position near the edge of the 50 mm disk. These cut samples are mounted in a temperature-controlled cell, oriented such that *xy*, *xz*, and *yz* planes are probed, respectively. The *x*-, *y*-, and *z*-axes correspond to the flow, shear gradient, and vorticity directions, respectively. Synchrotron

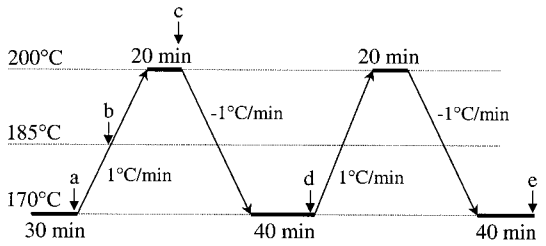

Figure 3. Schedule of the thermal history of the heating/cooling cycles for 2D-SAXS experiment. Images were taken at the following positions: (a) after alignment in the HEX (HEX-0), (b) in the HEX-BCC transition region (undulating HEX), (c) in the BCC phase (twinned BCC-I), (d) in the HEX region after the first cooling (HEX-I), and (e) in the HEX region after the second cooling (HEX-II).

SAXS measurements are performed in situ in the temperature cell as the system is heated and cooled through the OOT as indicated in Figure 3. The two-dimensional patterns are presented with a linear intensity scale (Figures 4 and 6).

Rheo-optical Measurements. Both the birefringence and the storage modulus, G', of a specimen during heating and cooling through the HEX−BCC transition were measured simultaneously with a rheo-optical device.[11] Here, the birefringence (Δn_{xz}) in the xz plane was measured by use of a polarization-modulation optical train, which enables rapid measurement of the magnitude and orientation of birefringence. The gap thickness used in the shear sandwich geometry was typically 0.3 mm, corresponding to an optical path length of 0.6 mm. For this optical path length, no indication of depolarization of light was observed for the initial, polydomain state (for which it would be most severe). Therefore, depolarization was neglected in the analysis of the data. After LAOS with $\omega = 1$ rad/s and 100% strain amplitude at 170 °C for 2.5 h until the birefringence and G' both reached steady-state values, repetitive heating and cooling experiments were conducted with small-amplitude, low-frequency dynamic shear (1% strain amplitude and 0.2 rad/s) to probe the mechanical properties of the sample while minimizing any potential effect of shear during HEX−BCC and BCC−HEX transitions. The heating and cooling rate was 0.33 °C/min.

Transmission Electron Microscopy. The microdomain structures of well-aligned HEX (point a in Figure 3) and of the first degenerated HEX (point d in Figure 3) were investigated by TEM after the sample was quenched with ice water. Cryogenic ultrasectioning was performed with an RMC (MT-700) cryomicrotome at −100 °C. A Hitachi transmission electron microscope operated at 75 kV was used to obtain micrographs of the specimens stained with OsO_4 for 7 min, which selectively stained the PI matrix black.

3. Results and Discussion

Alignment of the HEX Cylinders. Large-amplitude oscillatory shear was effective in inducing alignment of the HEX phase. The as-cast sample has nearly zero birefringence, indicating that there is no preferential HEX orientation. But within 100 s of shearing at 170 °C with a rim strain amplitude $\gamma_R = 100\%$ and a frequency $\omega = 1$ rad/s, the birefringence increased rapidly and G' decreased as the initially randomly oriented HEX grains of the as-cast sample of Vector 4111 became aligned along the shear direction.[3] After 100 s, both the birefringence and G' changed slowly (Figure 2). The orientation was very strong. The observed birefringence was close to theoretical predictions for a monodomain:[12] ~90% of the value based on form birefringence alone (see Appendix). The SAXS peaks observed in the xy and xz planes are very sharp (Figure 4); as a means to quantify the degree of orientation, we

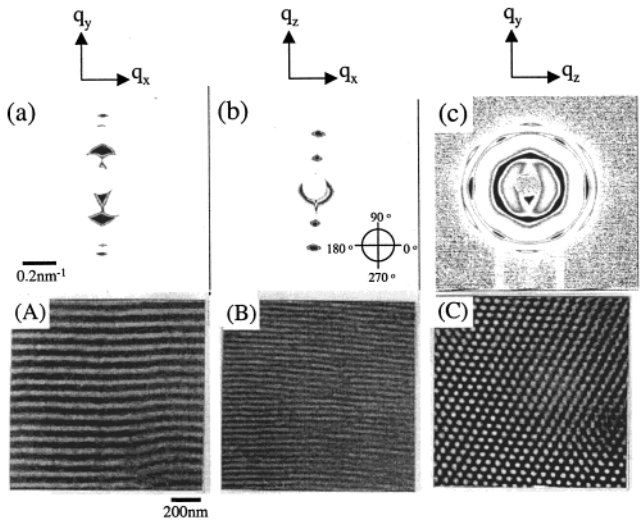

Figure 4. Strong alignment of the HEX cylinders in the flow direction after LAOS (HEX-0, position a in Figure 3) is confirmed by the 2D SAXS patterns and TEM images taken in three diffraction planes: (a, A) xy, (b, B) xz, and (c, C) zy planes. The 2-fold q_m and $2q_m$ peaks in the q_xq_y plane in panel a arise from the (100) plane seen in TEM (panel A), and the strong $\sqrt{3}q_m$ peak in the q_xq_z plane in panel b reflects the (110) plane of HEX seen in panel B, which implies that the cylinders are well aligned with the (100) plane of the HEX cylinders parallel to the xz plane [on the basis of the relative intensity of the first-order peaks in the q_xq_y and q_xq_z planes, there is less than 10% of the (110) orientation]. The hexagonal structure in the zy plane of panel C is in good agreement with the SAXS pattern (panel c).

evaluate an orientation factor in both the xy and xz planes[13]

$$F = -[3\langle\cos^2\theta\rangle - 1] \tag{1}$$

where

$$\langle\cos^2\theta\rangle = \frac{\int_0^\pi I(\theta)\cos^2\theta\sin\theta\,\mathrm{d}\theta}{\int_0^\pi I(\theta)\sin\theta\,\mathrm{d}\theta} \tag{2}$$

θ is as indicated in Figure 4b (the peak intensity is along $\pi/2$ and $3\pi/2$, which leads to the factor of -2 in eq 1 relative to the more familiar expression for nematic order oriented along 0 and π), and $I(\theta)$ is evaluated at the first-order peak in the xy plane for the {100} plane and at the second-order peak in the xz plane for the {110} plane, respectively. In the xy plane $F = 0.90$, and in the xz plane $F = 0.88$. (If the finite smearing due to the instrument were taken into account, a higher value would be obtained.) TEM images also confirm that a high degree of alignment has been induced (Figure 4). We refer to this initially aligned state as HEX-0.

Formation of the Twinned BCC. The transition from oriented HEX-0 to the first-generation twinned BCC-I is manifested in the mechanical and optical properties and the SAXS pattern. Upon first heating from HEX-0, the storage modulus of the aligned sample of Vector 4111 first increases gradually between 170 and 182 °C, then increases sharply from 182 to 190 °C, before leveling off (Figure 5). The 2D SAXS results (Figure 6a−c) indicate that the initial increase of G' coincides with the growth of undulations on the cylinders. As undulations grow, the intense $2q_m$ peaks of the well-aligned HEX (Figure 4a) disappear and weak

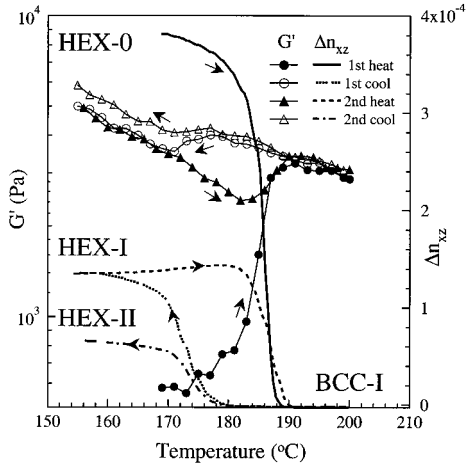

Figure 5. Repeated temperature sweeps of G' and Δn_{xz} with $\omega = 0.2$ rad/s and $\gamma_0 = 1\%$ at a ramping rate of 0.33 °C/min starting from the HEX-0 initial condition with no holding period at the upper and lower temperatures.

$\sqrt{2}q_m$ peaks appear (Figure 6a). The HEX to BCC transition temperature (T_{OOT}) of Vector 4111 is 185 ± 1 °C, as determined from synchrotron SAXS experiments during heating at a rate of 1 °C/min for HEX-0.[14] Thus, the strong increase in G' around 185 °C coincides with the complete splitting of undulating cylinders into spheres,[15,16] forming a twinned BCC (Figures 6d−f and 12). These behaviors are consistent with the results in ref 3. In the same temperature range, Δn_{xz} decreased slowly with the formation of undulating cylinders and then decreased precipitously to zero as the undulating cylinders split into spheres at T_{OOT} (Figure 5). The twinned BCC obtained from HEX-0 upon heating is denoted BCC-I.

Proliferation of Cylinder Orientations from Successively Twinned BCC. A distinctly different orientation distribution (HEX-I) is observed upon returning to the HEX state from BCC-I compared to the initial aligned state HEX-0. The transition from the twinned BCC-I to HEX-I during the first cooling occurs at ~172 °C (Figure 5), well below T_{OOT}, consistent with prior studies.[6,7,14] This can be explained by the existence of a kinetic barrier for merging the spheres.[7,16] Once spheres merge into cylinders during the cooling process, the modulus drops and the birefringence increases; interestingly, Δn_{xz} reaches only one-third that of the initially aligned HEX sample, while G' in the new HEX state becomes 1 order of magnitude higher than that of the initially aligned HEX sample (Figure 5). These results suggest that some of the cylinders have changed orientation from the initial shear direction.

The 2D SAXS patterns provide more direct evidence of the emergence of new cylinder orientations. The SAXS patterns in both q_xq_y and q_xq_z planes (Figure 6g,h) for HEX-I are completely different from those obtained for HEX-0 (Figure 4a,b). The $\sqrt{3}q_m$ high order peaks in Figure 6g−i confirm that the structure is that of the HEX phase. The positions of the q_m peaks in the three reflection planes in Figure 6g−i are similar to those of the twinned BCC-I at 200 °C in Figure 6d−f, even though the higher order peaks at $\sqrt{2}q_m$ have disappeared. The similarity in the first-order peaks indicates that the orientation of the {100} planes of the HEX lattice coincide with the directions of the {110} planes of the BCC lattice for all three reflection planes. Equivalently, the spheres along the ⟨111⟩ direction of

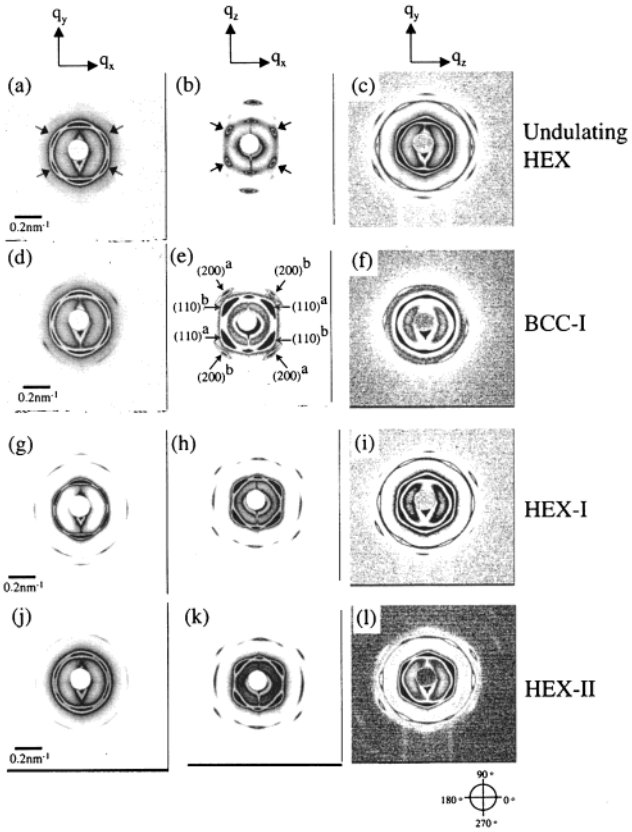

Figure 6. (a−c) Two-dimensional SAXS patterns at the HEX−BCC transition temperature (undulating HEX, point b in Figure 3) show four new peaks indicated by the arrows in both (a) q_xq_y and (b) q_xq_z planes due to the fluctuation of undulating cylinders.[21−24] (The real space illustration of undulating cylinders is shown in ref 22.) (d−f) Two-dimensional SAXS patterns of BCC-I (point c in Figure 3) are characteristic of a twinned BCC. The distinct appearance of four $\sqrt{2}q_m$ peaks in (e) q_xq_z are from the $(200)^a$ and $(200)^b$ planes (Figure 12a) of the twinned BCC structure.[25] The strong 2-fold q_m peaks along the q_y axis in (d) q_xq_y are from the reflections of $(110)^f$ and $(110)^g$ planes belonging to each twin (Figure 12b).[26] The clear 6-fold patterns at q_m and $\sqrt{2}q_m$ in (f) q_zq_y indicate that the cylinders split into BCC spheres along the ⟨111⟩ direction. (g−i) Two-dimensional SAXS patterns of HEX-I state at 170 °C after the first cooling (point d in Figure 3). (j−l) Two-dimensional SAXS patterns of HEX-II at 170 °C after the second cooling (point e in Figure 3).

the BCC lattice have been connected to form the axes of the new HEX phase, in accord with the so-called epitaxial relationship between BCC and HEX.[1−3,5−7,17] The TEM micrograph in Figure 7 in the xy plane after the first cooling also reveals cylinder orientations other than the original aligned cylinder direction indicated by the arrow. Therefore, we infer that the seven degenerate HEX states that can be created with their cylinder axes along the seven ⟨111⟩ directions of a twinned BCC (Figure 1) are indeed formed upon the transition from BCC-I to HEX-I.

Each of these seven, locally-aligned HEX states obtained after the first cooling upon repeated heating and cooling will produce a twinned BCC again with further proliferation of more HEX orientations in the second cooling. The process thus has a treelike structure (Figure 8). The further decrease in Δn_{xz} and increase in G' during the second cooling process (Figure 5) indicate this continued proliferation of HEX orientations. The SAXS patterns shown in Figure 6j−l after the second cooling (at point e in Figure 3) are similar

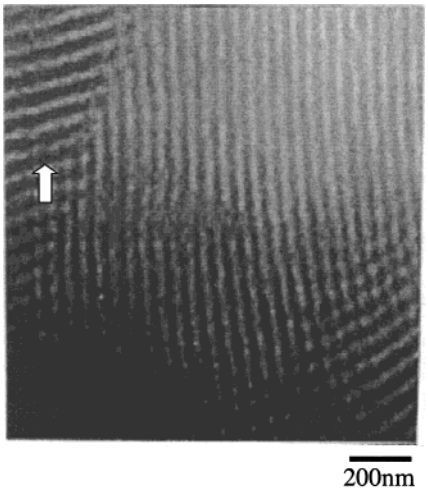

Figure 7. TEM micrograph of HEX-I taken in the *xy* plane. The white arrow points at cylinders having the initial HEX cylinder direction.

to those after the first cooling, although the scattering peaks show weaker intensity than those of the first cooling. The positions of the SAXS peaks of the first and second generation (HEX-I and HEX-II, respectively) agree well with the patterns expected for Bragg diffraction from the corresponding ensembles of HEX orientations (e.g., azimuthal plots of the first-order peaks, Figure 9a). The calculated SAXS patterns reveal the reason that HEX-I and HEX-II have similar scattering patterns (Figure 9b): the seven orientations present in HEX-I give the predominant contribution to the scattering in the *xy*, *xz*, and *yz* planes for HEX-II as well. However, the intensity is lower for HEX-II since some (roughly $^{9}/_{32}$) of the material is distributed among the other 18 orientations present in HEX-II (Figure 8). The accord between observed and calculated patterns suggests that the same epitaxial relationship holds for the second cooling as well.

Repeated heating/cooling cycles lead to further proliferation of new cylinder orientations, which is manifested in smearing of the SAXS profiles. As is clear from Figure 9a, the azimuthal intensity distribution approached a nearly isotropic state after nine heating/cooling cycles.

Memory of the Preceding HEX State. The cylinder axes of the seven degenerate HEX states in the first generation are determined from the corresponding ⟨111⟩ directions in the twinned BCC; however, the relative amounts of the distinct orientations in HEX-I appear not to be proportional to the corresponding ⟨111⟩ orientations in BCC-I. The SAXS patterns show that the orientation corresponding to HEX-0 is overrepresented in HEX-I compared to a calculation that gives each of the seven orientations a weighting in proportion to the corresponding ⟨111⟩ orientation in BCC-I (indicated in Figure 8): the relative intensity of the peaks at 90° and 270° is higher in the observed SAXS pattern (Figure 9a, first generation) than in the calculated pattern (Figure 9b, first generation). A bias in favor of the orientation of HEX-0 would also explain why a nonzero birefringence is observed for HEX-I: if the seven orientations in HEX-I were present in proportion to the corresponding ⟨111⟩ directions, the material would retain on average the cubic symmetry present in BCC-I, and the birefringence would be zero for HEX-I and all subsequent HEX generations. Indeed, we can use the observed birefringence in HEX-I to estimate the preference for HEX-0 over the other six orientations; and we can use the birefringence of HEX-II to see whether this

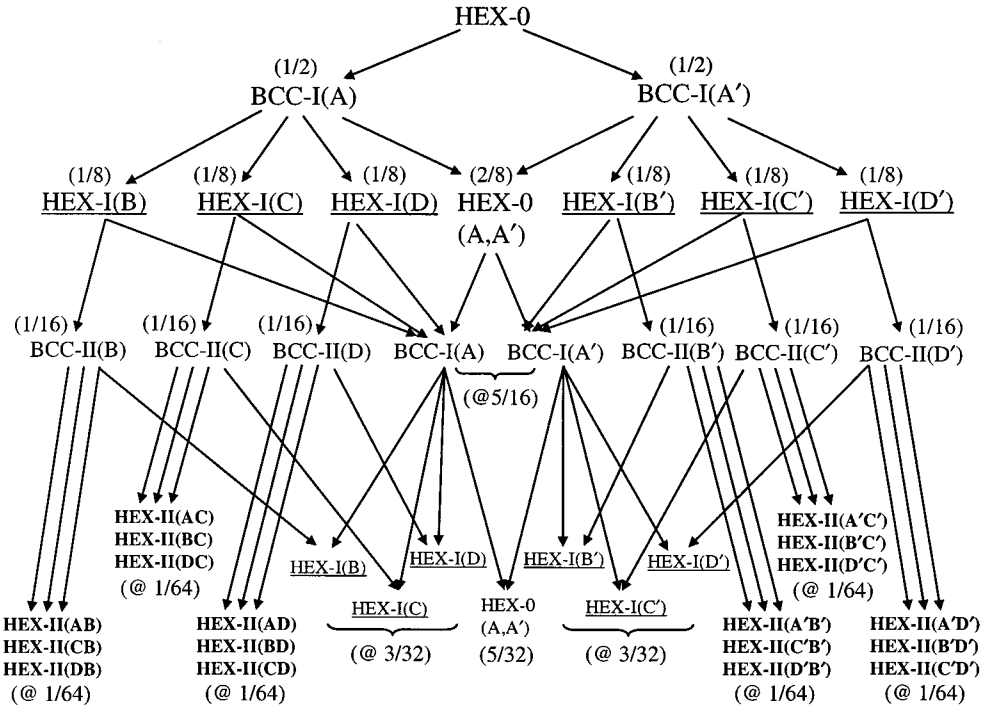

Figure 8. Proliferation of HEX orientations upon the first and second cooling (volume fractions indicated in parentheses are for the case that all the ⟨111⟩ orientations of each BCC are equally likely to produce corresponding HEX orientations). The underlined HEX entries are six newly formed orientations from the first cooling (HEX-I), and those shown in boldface type are 18 new ones formed upon the second cooling (HEX-II). Upon heating through the HEX → BCC transition, each HEX orientation gives rise to two BCC twins, one of which is the BCC twin that produced the particular HEX orientation in the preceding BCC → HEX transition. Upon cooling through the BCC → HEX transition, each BCC twin produces four HEX orientations, one of which is the HEX from which that particular twin came in the preceding HEX → BCC.

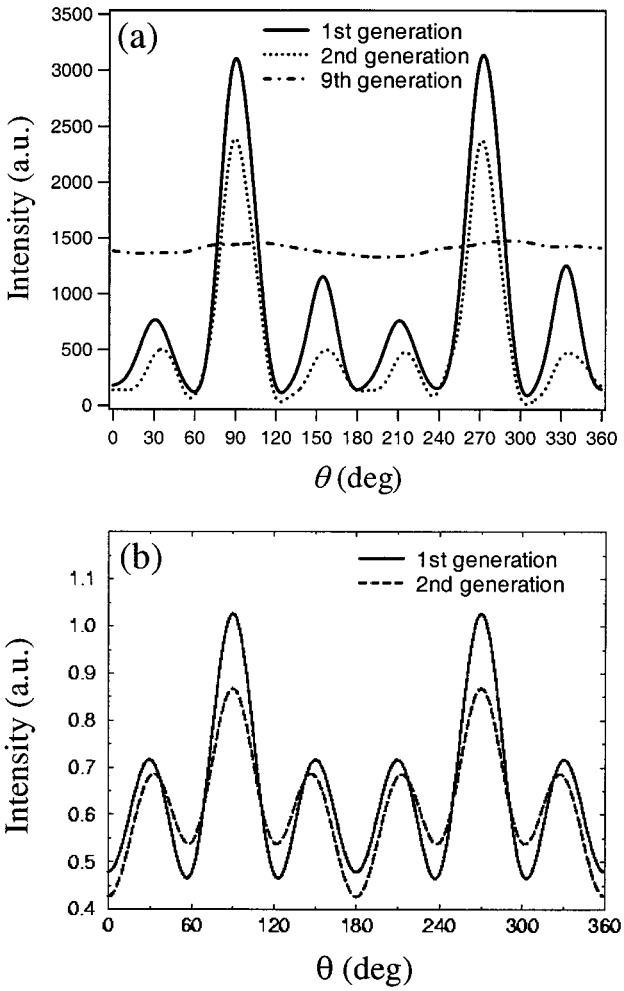

Figure 9. Change in the scattering intensity of first-order peaks with proliferation of new HEX directions in the q_xq_y plane: (a) SAXS experiment and (b) calculated azimuthal intensity distribution. The calculation assumes Gaussian peaks whose width is determined from the SAXS data for HEX-0.

preference for the orientation of "the HEX from which you came" holds for subsequent generations, as well.

The birefringence of an ensemble of HEX orientations can be computed given the direction and relative amounts of the various orientations. In HEX-I, the orientations are those of the ⟨111⟩ directions in the two twins present in BCC-I. Both twins have a ⟨111⟩ direction along the flow direction, denoted $\mathbf{e}_A$. In addition, each twin contributes three more orientations, denoted ($\mathbf{e}_B$, $\mathbf{e}_C$, $\mathbf{e}_D$) and ($\mathbf{e}_{B'}$, $\mathbf{e}_{C'}$, $\mathbf{e}_{D'}$) (Figure 13). If the unit vector $\mathbf{e}_A$ is set to $(1/\sqrt{3})(111)$, the vector components of the degenerate orientations of HEX-I are those given in Table 2 (calculated as described in the Appendix). The six new cylinder orientations obtained upon first cooling from twinned BCC-I are underlined in Figure 8.

In the next generation (HEX-I to BCC-II to HEX-II), each of the seven vectors, $\mathbf{e}_A$, $\mathbf{e}_B$, $\mathbf{e}_C$, $\mathbf{e}_D$, $\mathbf{e}_{B'}$, $\mathbf{e}_{C'}$, and $\mathbf{e}_{D'}$, which are the cylinder orientations of HEX-I, produces another pair of BCC twins. For example, if we consider $\mathbf{e}_{D'}$ [HEX-I(D′) in Figure 8], one of the twins [BCC-I(A′) in Figure 8], has ⟨111⟩ directions of the twin in BCC-I that gave rise to the HEX along $\mathbf{e}_{D'}$ [i.e., BCC-I(A′)], and the other twin [BCC-II(D′) in Figure 8]—a new BCC—introduces three new ⟨111⟩ orientations, $\mathbf{e}_{A'D'}$, $\mathbf{e}_{B'D'}$, and $\mathbf{e}_{C'D'}$ (Figure 13). (The new orientation vectors for the second cycle are denoted $\mathbf{e}_{ij}$, indicating the ith orientation proliferated from $\mathbf{e}_j$.)

In this way, 18 new cylinder orientations in HEX-II are obtained from $\mathbf{e}_B$, $\mathbf{e}_C$, $\mathbf{e}_D$, $\mathbf{e}_{B'}$, $\mathbf{e}_{C'}$, and $\mathbf{e}_{D'}$ after the second cooling. The 18 newly proliferated HEX orientations upon the second cooling are shown in boldface type in Figure 8 (vectors are listed in Table 2). Indeed, none of these 18 vectors coincide with each other. Using these cylinder orientations, we can calculate the relative value of the birefringence in the xz plane, Δn_{xz}, of the degenerate HEX states relative to the birefringence of the initial well-aligned HEX-0, $\Delta n_{xz}^{\max}$ (see Appendix):

$$\Delta n_{xz}^{\text{eff}} = \Delta n_{xz}^{\max} \sum_{i=A}^{G} \nu_i(\cos^2\theta_i - \sin^2\theta_i \cos^2\varphi_i) \quad (3)$$

where ν_i is the volume fraction of HEX-i, and θ_i and φ_i are angles of the vector of the cylinder orientation i.

If all the ⟨111⟩ orientations are equally likely to produce HEX states with cylinders along their orientation, then the volume fractions of each orientation are those indicated in parentheses in Figure 8. In this case, $\Delta n_{xz}^{\text{eff}}$ becomes zero for the first and all subsequent HEX states, as mentioned above. Instead, the experimental data show considerable birefringence in HEX-I and HEX-II (Figure 5), reflecting the preference for the initial HEX orientation (HEX-A in Figure 1) evident in the SAXS pattern (Figure 9). The birefringence observed in HEX-I (Figure 5) is consistent with a 3−4-fold greater preference for the orientation of the HEX from which a given BCC came relative to the other HEX orientations formed in the BCC → HEX transition. For example, the birefringence of HEX-I is captured by eq 3 with ν_i ($i = A$) $\approx 3.3\nu_j$ ($j \neq A$). Further, the birefringence of HEX-II relative to HEX-I is also captured by a 3−4-fold bias factor when it is applied for each of the HEX orientations propagating forward from HEX-I through BCC-II to HEX-II.

To observe how the memory of the prior HEX orientation decays with time in the BCC state, we have measured the birefringence of HEX-I as a function of the annealing time in the twinned BCC-I. The birefringence of HEX-I decreases with increasing annealing time in the twinned BCC-I, both for an SI diblock copolymer having a HEX−BCC transition (Figure 10) and for the SIS triblock. The two types of systems show similar HEX-I structure in both SAXS and rheo-optical experiments as functions of annealing time in BCC-I. The bias factor observed for the case of no annealing in the BCC phase was similar for the diblock (3.8 for SI-C1 in Figure 10) and triblock (3.3 for Vector 4111 in Figure 5).

Since the relative change in birefringence is used to infer the bias factor, it represents a fairly robust estimate. The analysis is not affected by the lack of a quantitative model for the value of the birefringence of a HEX monodomain.[18] Small imperfections of the initial alignment of HEX-0 have little effect on the estimate, since a small but finite breadth of the initial orientation distribution cancels out of the birefringence ratio. We do not detect depolarization of light by our polydomain samples; if it were significant, the actual bias factor could be larger than inferred by this method.

Why Has HEX Proliferation Not Been Reported Before? We now contrast our findings with those of Koppi et al.[1] and Kimishima et al.[8] Koppi et al.[1] studied

Table 2. New Cylinder Directions from ⟨111⟩ Directions of First and Second Twinned BCCs[a]

HEX-I (θ,φ)	$\mathbf{e}_B$ $\frac{1}{\sqrt{3}}(1\bar{1}\bar{1})$ (109.47,120)	$\mathbf{e}_C$ $\frac{1}{\sqrt{3}}(\bar{1}1\bar{1})$ (109.47,**240**)	$\mathbf{e}_D$ $\frac{1}{\sqrt{3}}(\bar{1}\bar{1}1)$ (109.47, 0)	$\mathbf{e}_{B'}$ $\frac{1}{\sqrt{3}}(\frac{\bar{5}}{3}\frac{1}{3}\frac{1}{3})$ (109.47, **300**)	$\mathbf{e}_{C'}$ $\frac{1}{\sqrt{3}}(\frac{1}{3}\frac{\bar{5}}{3}\frac{1}{3})$ (109.47, 60)	$\mathbf{e}_{D'}$ $\frac{1}{\sqrt{3}}(\frac{1}{3}\frac{1}{3}\frac{\bar{5}}{3})$ (109.47,180)
	$\mathbf{e}_{AB}$ $\frac{1}{\sqrt{3}}(\frac{\bar{5}}{3}\frac{1}{3}\frac{1}{3})$ (141.06, **300**)	$\mathbf{e}_{AC}$ $\frac{1}{\sqrt{3}}(\frac{\bar{1}}{3}\frac{5}{3}\frac{1}{3})$ (141.06, 60)	$\mathbf{e}_{AD}$ $\frac{1}{\sqrt{3}}(\frac{\bar{1}}{3}\frac{1}{3}\frac{5}{3})$ (141.06, 180)	$\mathbf{e}_{A'B'}$ $\frac{1}{\sqrt{3}}(\frac{1}{9}\frac{\bar{1}}{9}\frac{1}{9}\frac{1}{9})$ (141.06, 120)	$\mathbf{e}_{A'C'}$ $\frac{1}{\sqrt{3}}(\frac{\bar{1}}{9}\frac{1}{9}\frac{\bar{1}}{9}\frac{1}{9})$ (141.06, **240**)	$\mathbf{e}_{A'D'}$ $\frac{1}{\sqrt{3}}(\frac{\bar{1}}{9}\frac{\bar{1}}{9}\frac{1}{9}\frac{1}{9})$ (141.06, 0)
HEX-II (θ,φ)	$\mathbf{e}_{CB}$ $\frac{1}{\sqrt{3}}(\frac{1}{3}\frac{\bar{1}}{3}\frac{5}{3})$ (56.25, 19.1)	$\mathbf{e}_{BC}$ $\frac{1}{\sqrt{3}}(\frac{\bar{1}}{3}\frac{1}{3}\frac{5}{3})$ (56.25, **340.9**)	$\mathbf{e}_{BD}$ $\frac{1}{\sqrt{3}}(\frac{\bar{1}}{3}\frac{5}{3}\frac{1}{3})$ (56.25, **259.1**)	$\mathbf{e}_{C'B'}$ $\frac{1}{\sqrt{3}}(\frac{7}{9}\frac{13}{9}\frac{\bar{5}}{9})$ (56.25, **199.1**)	$\mathbf{e}_{B'C'}$ $\frac{1}{\sqrt{3}}(\frac{13}{9}\frac{7}{9}\frac{\bar{5}}{9})$ (56.25, 160.9)	$\mathbf{e}_{B'D'}$ $\frac{1}{\sqrt{3}}(\frac{13}{9}\frac{\bar{5}}{9}\frac{7}{9})$ (56.25, 79.1)
	$\mathbf{e}_{DB}$ $\frac{1}{\sqrt{3}}(\frac{1}{3}\frac{5}{3}\frac{\bar{1}}{3})$ (56.25,139.1)	$\mathbf{e}_{DC}$ $\frac{1}{\sqrt{3}}(\frac{5}{3}\frac{1}{3}\frac{\bar{1}}{3})$ (56.25, **220.9**)	$\mathbf{e}_{CD}$ $\frac{1}{\sqrt{3}}(\frac{5}{3}\frac{\bar{1}}{3}\frac{1}{3})$ (56.25, **100.9**)	$\mathbf{e}_{D'B'}$ $\frac{1}{\sqrt{3}}(\frac{7}{9}\frac{\bar{5}}{9}\frac{13}{9})$ (56.25, **319.1**)	$\mathbf{e}_{D'C'}$ $\frac{1}{\sqrt{3}}(\frac{\bar{5}}{9}\frac{7}{9}\frac{13}{9})$ (56.25, 40.9)	$\mathbf{e}_{C'D'}$ $\frac{1}{\sqrt{3}}(\frac{\bar{5}}{9}\frac{13}{9}\frac{7}{9})$ (56.25, **280.9**)

[a] Each e_{ij} of HEX-II is proliferated from e_i of HEX-I. The θ and φ are the angles defined in Figure 1, taking e_A and $\hat{e}_z$ in Figure 13 to be the unit vectors of x and z, respectively.

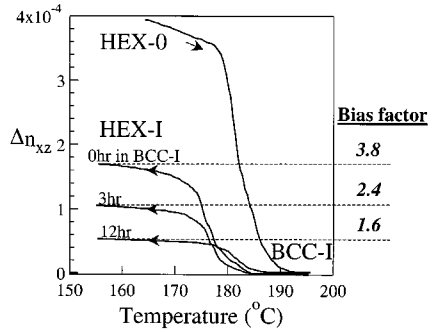

Figure 10. Effect of annealing in the twinned BCC state on Δn_{xz} of HEX-I for SI-C1 diblock copolymer.

the HEX to BCC to HEX transition in a PEP−PEE diblock copolymer with PEP cylinder domains (f_{PEP} = 0.25) using dynamic shear (2% strain amplitude and 0.5 rad/s) during heating and cooling at a rate of 1 °C/min, with no annealing in the BCC state. Upon the reverse transition from BCC to HEX, the modulus of the new HEX essentially returned to that of the initial aligned HEX. In contrast to Figure 5, this lack of change in the modulus of the HEX phase from the initial aligned HEX indicates that the orientation distribution in their first-generation HEX with a short dwell time in the BCC phase (no annealing) is similar to the initial aligned HEX orientation distribution. Kimishima et al.,[8] using a polydomain, ordered SI diblock copolymer, also observed that the original cylinder orientation was recovered in each grain following the HEX to BCC to HEX transitions, even when the sample was annealed for an hour in the BCC state. As we have described, there is a memory effect of the prior HEX orientation that persists for some time in the BCC phase. We infer that in both prior studies, the residence time in the BCC state was short compared to the memory decay time of their materials.

It is reasonable to hypothesize that the decay times of the prior materials could be much longer than observed in the present materials (several hours, Figure 10). In the case of Koppi et al.,[1] the high degree of entanglement (N_{PEP}/Ne_{PEP} of 12 and N_{PEE}/Ne_{PEE} of 6.6) could result in slower relaxation than the present system (SI diblock with N_{PS}/Ne_{PS} of 0.7 and N_{PI}/Ne_{PI} of 8.3).[19] In the case of Kimishima et al.,[8] proximity of the experimental temperatures (T_{OOT} of 116 °C, T_{anneal} of 120 °C) to the T_g of the PS-rich domains (∼80 °C) could result in slower relaxation than our material, SI diblock (T_{OOT} of 182 °C, T_{anneal} of 190 °C).[14]

The nature of the memory effect and, consequently, the mechanism for its relaxation are not known. Kimishima et al.[8] speculate that there is some anisotropy in the BCC structure reflecting the HEX orientation from which it came. If such an anisotropy is present, it is below the detection limit of SAXS. Also, since the anisotropy they suggest is on nanoscopic length scales, it would be expected to relax rapidly (on the time scale for redistribution of S−I junctions over the surface of an individual spherical domain). Alternatively, Matsen[17] suggested that the poor correlation of spheres originating from different rupturing cylinders in both time and space cause the memory effect. However, we did not observe a sharpening or an increase in intensity of the BCC diffraction peaks with time in the BCC phase.[14] Further studies of the transient structure in the BCC state are needed to determine the physical basis of the memory effect.

4. Conclusions

In this work, the thermally reversible HEX−BCC transition was examined through several repeated heating/cooling cycles. A key finding of our study is the orientational proliferation of the HEX phase and successive twinning of the BCC during these cycles. This unique phenomenon is a consequence of two crucial mechanisms in the HEX−BCC transition, the epitaxial relationship and the generation of a twinned, rather than a single, BCC from the HEX phase. These two mechanisms dictate that, starting from an initially aligned HEX, seven cylinder orientations (including the initial one) are created after the first heating/cooling cycle and 25 cylinder orientations (including the seven present in HEX-I) are generated after the second cycle. Two-dimensional SAXS, rheo-optics, and TEM results are fully consistent with these mechanisms. The nonzero birefringence of HEX-I suggests a preference for the cylinder orientation in the initially shear-aligned direction, which indicates some memory of the initially aligned HEX state. This memory effect is shown to decrease with annealing time in the twinned BCC state. Differences in the memory effects between our system and those of previous studies may be responsible for the fact that previous studies did not observe the orientational proliferation and successive twinning reported in our work.

Acknowledgment. We acknowledge helpful discussions with Professors T. Hashimoto, T. Lodge, S. Okamoto, C. Y. Ryu, S. Sakurai and A. C. Shi. This work was supported by KOSEF (97-05-02-03-01-3), by the Applied Rheology Center governed by KOSEF (2000 G0202), by TND projects supported by the Ministry of Science and Technology (MOST) and by NSF (CTS-9729443) and AFOSR (LC MURI). Synchrotron SAXS at the PLS (3C2 and 4C1 beam lines) was supported by MOST and Pohang Iron and Steel Co. (POSCO). Vector 4111 was kindly provided by Professor C. D. Han at the University of Akron.

Appendix: Derivation of Δn_{xz} from the Lorentz−Lorenz Equation

For a single-crystal-like HEX cylindrical microdomain, the form birefringence in the plane of the flow and vorticity directions, Δn_{xz}, was estimated by[12]

$$\Delta n_{xz} = n_x - n_z = \frac{v_{PS} v_{PI} (n_{PS}^2 - n_{PI}^2)^2}{2 n_a [(v_{PS} + 1) n_{PI}^2 + v_{PI} n_{PS}^2]} \quad \text{(A1)}$$

where v_i is the volume fraction of the i block, $n_a^2 = v_{PS} n_{PS}^2 + v_{PI} n_{PI}^2$, and n_i is the bulk refractive indices of species i ($n_{PS} = 1.59$ and $n_{PI} = 1.52$). This equation assumes strong segregation, leading one to expect the actual form birefringence to be smaller than this estimate. On the other hand, this equation neglects the intrinsic birefringence, which is expected to increase the birefringence in the case of PS cylinders in a PI matrix (PS more stretched than PI),[18] leading one to expect the actual birefringence (form + intrinsic) to be larger than the form estimate alone. It appears that these two errors approximately cancel out, since the agreement between the estimate from eq A1 and experimentally observed values for well-aligned styrene−diene cylinders was found to be surprisingly good (calculated value was 6% higher than the observed value).[12] From eq A1, with the volume fraction of each block $v_{PS} = 0.16$ and $v_{PI} = 0.84$ at 170 °C, Δn_{xz} of perfectly oriented Vector 4111 is predicted to be 4.3×10^{-4}. A theoretical attempt to account for the intrinsic birefringence of a related styrene−diene HEX[18] led to an unphysical result (theoretical prediction for the intrinsic contribution was much larger than the observed Δn); thus, it is not possible for us to compare to a theoretical result that accounts for both form and intrinsic contributions.

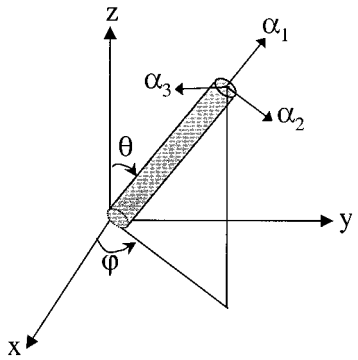

Figure 11. Coordinate system of an anisotropic cylinder and polarizability components.

Orientation distributions other than monodomain order result in lower values of the birefringence. These relative changes can be treated in a robust way that gives the approximate ratio of the birefringence for a new orientation distribution to that of a monodomain. These predicted ratios can be compared to observed ratios to obtain a result that is insensitive to imperfect orientation of the actual HEX-0 state and to cancel out inaccuracies of the existing models for the birefringence of the HEX phase. We can estimate Δn_{xz} from the polarizability tensor for an anisotropic material using the Lorentz−Lorenz equation.[20] In Figure 11, the coordinate system for an anisotropic cylinder is depicted. The induced dipole $\boldsymbol{p}$ is calculated from the following empirical relationship:

$$\boldsymbol{p} = \underline{\underline{\alpha}} \boldsymbol{E} \quad \text{(A2)}$$

where $\boldsymbol{E}$ is the incident electric field. For an anisotropic material, the polarizability is a tensor that depends on the relative orientation of the principal axes of the material and the incident electric field. If the polarizability is biaxial and of the form

$$\underline{\underline{\alpha}} = \begin{pmatrix} \alpha_3 & 0 & 0 \\ 0 & \alpha_2 & 0 \\ 0 & 0 & \alpha_1 \end{pmatrix} \quad \text{(A3)}$$

each polarizability component can be expressed in terms of the laboratory frame, e_x, e_y, e_z in Figure 11.

$$\alpha_1 = (\cos\varphi \sin\theta) e_z + (\sin\varphi \sin\theta) e_y + (\cos\theta) e_x \quad \text{(A4)}$$

$$\alpha_2 = (\cos\varphi \cos\theta) e_z + (\sin\varphi \cos\theta) e_y - (\sin\theta) e_x \quad \text{(A5)}$$

$$\alpha_3 = (\sin\varphi) e_z - (\cos\varphi) e_y \quad \text{(A6)}$$

Therefore

$$\begin{pmatrix} \alpha_3 \\ \alpha_2 \\ \alpha_1 \end{pmatrix} = \begin{pmatrix} \sin\varphi & -\cos\varphi & 0 \\ \cos\theta\cos\varphi & \cos\theta\sin\varphi & -\sin\theta \\ \sin\theta\cos\varphi & \sin\theta\sin\varphi & \cos\theta \end{pmatrix} \begin{pmatrix} e_z \\ e_y \\ e_x \end{pmatrix} \quad \text{(A7)}$$

Applying rotation matrixes defined in eq A7 to $\underline{\underline{\alpha}}$ and the uniaxial symmetry of cylinders ($\alpha_2 = \alpha_3$)

$$\underline{\underline{\alpha}}(\theta,\varphi) = \begin{pmatrix} \sin\varphi & \cos\theta\cos\varphi & \sin\theta\cos\varphi \\ -\cos\varphi & \cos\theta\sin\varphi & \sin\theta\sin\varphi \\ 0 & -\sin\theta & \cos\theta \end{pmatrix} \begin{pmatrix} \alpha_2 & 0 & 0 \\ 0 & \alpha_2 & 0 \\ 0 & 0 & \alpha_1 \end{pmatrix} \begin{pmatrix} \sin\varphi & -\cos\varphi & 0 \\ \cos\theta\cos\varphi & \cos\theta\sin\varphi & -\sin\theta \\ \sin\theta\cos\varphi & \sin\theta\sin\varphi & \cos\theta \end{pmatrix} =$$

$$\alpha_2 I + (\alpha_1 - \alpha_2) \begin{pmatrix} \cos^2\varphi\sin^2\theta & \cos\varphi\sin\varphi\sin^2\theta & \cos\varphi\sin\theta\cos\theta \\ \cos\varphi\sin\varphi\sin^2\theta & \sin^2\varphi\sin^2\theta & \sin\varphi\sin\theta\cos\theta \\ \cos\varphi\sin\theta\cos\theta & \sin\varphi\sin\theta\cos\theta & \cos^2\theta \end{pmatrix} \quad \text{(A8)}$$

Therefore

$$\alpha_{zz} = \alpha_2 + (\alpha_1 - \alpha_2)\sin^2\theta\cos^2\varphi \quad \text{(A9)}$$

$$\alpha_{xx} = \alpha_2 + (\alpha_1 - \alpha_2)\cos^2\theta \quad \text{(A10)}$$

From the Lorentz−Lorenz equation:

$$\frac{{n_{xx}}^2 - 1}{{n_{xx}}^2 + 2} = \frac{4\pi}{3}\alpha_{xx} \quad \text{(A11)}$$

$$\frac{{n_{zz}}^2 - 1}{{n_{zz}}^2 + 2} = \frac{4\pi}{3}\alpha_{zz} \quad \text{(A12)}$$

The birefringence Δn_{xz} and the average refractive index $\bar{n}$ are defined as follows:

$$\Delta n_{xz} = n_{xx} - n_{zz} \quad \text{(A13)}$$

$$\bar{n} = {}^1/_2(n_{xx} + n_{zz}) \quad \text{(A14)}$$

Then

$$n_{xx} = \bar{n} + (\Delta n_{xz}/2) \quad \text{(A15)}$$

$$n_{zz} = \bar{n} - (\Delta n_{xz}/2) \quad \text{(A16)}$$

Subtraction of eq A12 from eq A11 yields

$$\frac{{n_{xx}}^2 - 1}{{n_{xx}}^2 + 2} - \frac{{n_{zz}}^2 - 1}{{n_{zz}}^2 + 2} = \frac{6\bar{n}\Delta n_{xz}}{({n_{xx}}^2 + 2)({n_{zz}}^2 + 2)} \approx$$

$$\frac{6\bar{n}\Delta n_{xz}}{(\bar{n}^2 + 2)^2} = \frac{4\pi}{3}(\alpha_1 - \alpha_2)(\cos^2\theta - \sin^2\theta\cos^2\varphi) \quad \text{(A17)}$$

Therefore

$$\Delta {n_{xz}}^{\text{eff}} \approx \frac{2\pi(\bar{n}^2 + 2)^2}{9\bar{n}}(\alpha_1 - \alpha_2)(\cos^2\theta - \sin^2\theta\cos^2\varphi) \approx \Delta {n_{xz}}^{\max}(\cos^2\theta - \sin^2\theta\cos^2\varphi) \quad \text{(A18)}$$

The orientation angles θ and φ of the distinct HEX orientations are determined from the geometry of the BCC twins. There are four ⟨111⟩ directions in each twin present in BCC-I, but the one along the x direction (initial shear direction) is shared by both (Figure 12b). The unit vector of the ⟨111⟩ direction that coincides with the cylinder axes of the original aligned HEX is denoted $\mathbf{e}_A$. The other three ⟨111⟩ vectors in one of the twins ($\mathbf{e}_B$, $\mathbf{e}_C$, $\mathbf{e}_D$) correspond to the bonds of a diamond tetrahedron skeleton with the angle between the bonds being 109.47° (Figure 13). The other three orientations, $\mathbf{e}_{B'}$, $\mathbf{e}_{C'}$, and $\mathbf{e}_{D'}$, comprising the other BCC twin can be obtained by respectively inverting $\mathbf{e}_B$, $\mathbf{e}_C$, and $\mathbf{e}_D$ and reflecting with respect to the plane normal to $\mathbf{e}_A$. Mathematically:

$$\mathbf{e}_{i'} = -\mathbf{e}_i + 2(\mathbf{e}_i \cdot \mathbf{e}_A)\mathbf{e}_A \qquad (i = \text{B, C, D}) \quad \text{(A19)}$$

as illustrated in Figure 13.

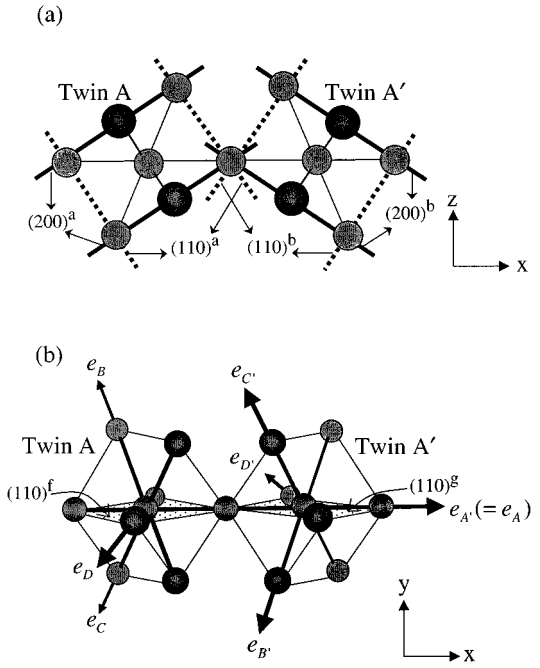

Figure 12. Reflection planes and ⟨111⟩ directions of a twinned BCC shown in (a) $x-z$ plane and (b) $x-y$ plane.

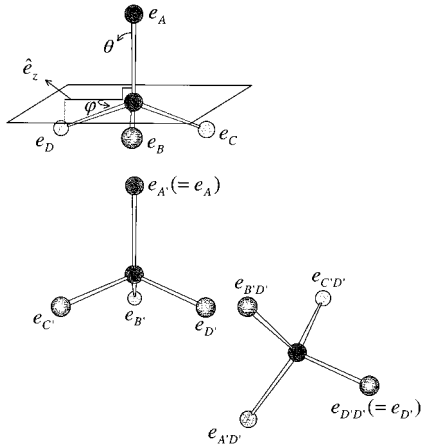

Figure 13. Determination of the cylinder orientations from the ⟨111⟩ directions of the twinned BCC. The $\hat{e}_z$ is the projected vector of e_D on the plane normal to e_A.

References and Notes

(1) Koppi, K. A.; Tirrell, M.; Bates, F. S.; Almdal, K.; Mortensen, K. *J. Rheol.* **1994**, *38*, 999.
(2) Sakurai, S.; Hashimoto, T.; Fetters, L. J. *Macromolecules* **1996**, *29*, 740.

(3) Ryu, C. Y.; Lee, M. S.; Hajduk, D. A.; Lodge, T. J. *Polym. Sci., Polym. Phys. Ed.* **1997**, *35*, 2811.
(4) Sakamoto, N.; Hashimoto, T.; Han, C. D.; Kim, D.; Vaidya, N. Y.; *Macromolecules* **1997**, *30*, 1621.
(5) Qi, S.; Wang, Z.-G. *Polymer* **1998**, *39*, 4639.
(6) Ryu, C. Y.; Vigild, M. E.; Lodge, T. P. *Phys. Rev. Lett.* **1998**, *81*, 5354.
(7) Ryu, C. Y.; Lodge, T. P. *Macromolecules* **1999**, *32*, 7190.
(8) Kimishima, K.; Koga, T.; Hashimoto, T. *Macromolecules* **2000**, *33*, 968.
(9) Kwon, K.; Lee, W.; Cho, D.; Chang, T. *Korea Polym. J.* **1999**, *7*, 321.
(10) Park, B. J.; Rah, S. Y.; Park, Y. J.; Lee, K. B. *Rev. Sci. Instrum.* **1995**, *66*, 1722.
(11) Kannan, R. M.; Kornfield, J. A. *Macromolecules* **1994**, *27*, 1177.
(12) Folkes, M. J.; Keller, A. *Polymer* **1971**, *12*, 222.
(13) Sakurai, S.; Aida, S.; Okamoto, S.; Ono, T.; Imaizumi, K.; Nomura, S. *Macromolecules* **2001**, *34*, 3672.
(14) Lee, H. H.; Kim, J. K. *ACS Symp. Ser.* **2000**, *739*, 470.
(15) Kim, J. K.; Lee, H. H.; Gu, Q.-J.; Chang, T.; Jeong, Y. H. *Macromolecules* **1998**, *31*, 4045.
(16) Kim, J. K.; Lee, H. H.; Ree, M.; Lee, K. B.; Park, Y. *Macromol. Chem. Phys.* **1998**, *199*, 641.
(17) Matsen, M. W. *J. Chem. Phys.* **2001**, *114*, 8165.
(18) Lodge, T. P.; Fredrickson, G. H. *Macromolecules* **1992**, *25*, 5643.
(19) Okamoto, H.; Inoue, T.; Osaki, K. *J. Polym. Sci.: Polym. Phys. Ed.* **1995**, *33*, 417.
(20) Fuller, G. G. *Optical Rheometry of Complex Fluids*; Oxford University Press: Oxford, U.K., 1997.
(21) Shi, A.-C.; Noolandi, J.; Desai, R. C. *Macromolecules* **1996**, *29*, 6487.
(22) Laradji, M.; Shi, A.-C.; Noolandi, J.; Desai, R. C. *Macromolecules* **1997**, *30*, 3242.
(23) Qi, S.; Wang, Z.-G. *Phy. Rev. Lett.* **1996**, *76*, 1670.
(24) Qi, S.; Wang, Z.-G. *Macromolecules* **1997**, *30*, 4491.
(25) Almdal, K.; Koppi, K. A.; Bates, F. S. *Macromolecules* **1993**, *26*, 4058.
(26) The four weak diagonal peaks of q_m at around 30°, 150°, 210°, and 330° in the q_xq_y plane in Figure 6a perhaps result from the overlap of residual intensity of the Gaussian Bragg peaks of the twinned BCC. These angles are slightly different from those (35°, 145°, 215°, and 325°) in the q_xq_z plane (Figure 6b), which are the positions where two rings intersect each other (i.e.,$\pm K_3$ and $\pm Q_3$ in Figure 3a of ref 5). When Bragg peaks are not Delta function but Gaussian type with a finite width, the intensity from the overlap of the residual tails of Bragg peaks from $\pm K_3$ and $\pm Q_3$ become a maximum at the positions at 30°, 150°, 210°, and 330° on q_xq_y. Alternatively, these weak peaks may reflect a small amount of oriented HEX with [110] orientation. We note that these four weak peaks in the q_xq_y plane were not reported in the SANS studies by Almdal et al.[25]

MA010951C